

Article

Microstructure Evolution and Mechanical Properties of Spark Plasma Sintered Manganese Addition on Ti-48Al-2Cr-2Nb Alloys

A. Raja Annamalai ^{1,†} , Muthe Srikanth ^{2,†} , Raunak Varshney ², Mehta Yash Ashokkumar ², Swarup Kumar Patro ² and Chun-Ping Jen ^{3,*} 

¹ Centre for Innovative Manufacturing Research, VIT, Vellore 632014, India; raja.annamalai@vit.ac.in

² School of Mechanical Engineering, VIT, Vellore 632014, India; muthe.srikanth@vit.ac.in (M.S.); varshneyraunak09@gmail.com (R.V.); romimehta1990@gmail.com or mehtayash.ashokkumar2014@vit.ac.in (M.Y.A.); swarupkumarpatro@gmail.com (S.K.P.)

³ Department of Mechanical Engineering, National Chung Cheng University, Chiayi 62102, Taiwan

* Correspondence: imecpj@ccu.edu.tw; Tel.: +886-5-2729-382; Fax: +886-5-2720-589

† Equally contributed as the first author.

Received: 5 November 2020; Accepted: 24 November 2020; Published: 25 November 2020



Abstract: Titanium aluminide (TiAl) is one of the most promising materials for aerospace applications. It is a suitable replacement for nickel-based superalloys predominantly used in these applications. Titanium aluminide with superior processability is the main task in carrying out this work. A less brittle TiAl alloy was fabricated using spark plasma sintering by adding the nominal composition (2.5, 5, and 7.5 wt.%) of manganese (Mn) to Ti-48Al-2Cr-2Nb. The samples were sintered at 1150 °C using spark plasma sintering (SPS), which helped produce highly dense models with fine grain sizes at the high heating rate (here, 100 °C per minute). The effects produced by Mn additions on the densification, mechanical properties (yield strength, hardness, and % elongation), and microstructure of the Ti aluminide alloys are studied. Scanning electron microscopy (SEM) has been used to explore the sintered samples' microstructures. The alloyed materials are entirely dissolved in the gamma matrix due to the manganese approaching its melting point. XRD and SEM analysis confirmed the new intermetallic related to Mn neither with titanium nor aluminum. The enhancement of % elongation at break is evident for the little improvement in the ductility of TiAl by the addition of Mn. The samples' tensile fracture nature is also evidence for enhancement in the alloy's % elongation.

Keywords: Ti-48Al-2Cr-2Nb; TiAl (γ); Ti₃Al (α_2); spark plasma sintering (SPS); yield strength; microstructures; tensile fracture

1. Introduction

In the automobile industry, power generators, and aircraft engines, titanium aluminides have overwhelming applications. Ti aluminides have demonstrated their significance in the alloy category, especially in the aviation industry. Extensive analysis was carried out over long periods on applying these alloys [1]. Ti-Al-based alloys, which include titanium aluminides, have attracted many researchers since they have good high-temperature performance and are lightweight. For example, a useful application of Ti-48Al-2Cr-2Nb is found in the blades of low-pressure turbines in aircraft engines. The properties of Ti aluminide alloys depend on the changes in the microstructure, the phases present (here, γ (TiAl) + α_2 (Ti₃Al)), and also on the type of sintering process and the cooling rate. The intermetallic phase γ (TiAl) has desirable high-temperature (>800 °C) properties, but at low temperatures is hindered due to its low-temperature ductility [2]. They are found to have fully lamellar structures, which exhibit low ductility [3]. It has been found that with the addition of β

stabilizers such as Mn and Sn into Ti aluminide, the room-temperature ductility can be improved [4]. Titanium aluminide alloys have low ductility under room-temperature conditions. Thus, they tend to fracture very quickly under the application of tensile or compressive forces. It has been found that more remarkable plasticity of these two-phased ($\gamma + \alpha_2$) alloys can be achieved by adding other elements, which introduce a new phase in the alloy, and using microstructure modification. A standard method that has been developed recently to optimize the properties of Ti aluminide-based alloy is refining the microstructure, i.e., reduce or refine the grain size with controlled grain growth, as it may improve, quite substantially, the ductility at ambient conditions, without downgrading its creep resistance [5]. Hence, TiAl alloys with other β -stabilizing elements are being considered as an excellent method to uplift the material properties of Ti aluminides. Due to the relative % elongation of TiAl-based alloys, their production is challenging. Powder metallurgy is a state-of-the-art method for synthesizing ultra-fine grain alloys [6]. Spark plasma sintering (SPS) is a novel fabrication technique for TiAl-based alloys due to the near-net-shape properties, utilization level of materials, and the ability to fabricate highly homogenous microstructures with uniform chemical compositions. One must include parameters in the spark plasma sintering process to achieve near solidus or complete densification using a correct combination of temperature and pressure (here, 1150 °C and 30 MPa). The difficulty is to achieve a pore-free and homogeneous microstructure, particularly in titanium and its alloy. It is noted that pre-alloyed powder is preferred over separate elemental powdered blends for the following reasons: (i) due to the chemical inhomogeneity produced if blended from different powders during the sintering process; and (ii) diffusion of particles of aluminum in the lattice by Kirkendall-type voids that usually emerge [7]. Aluminide-based alloys using β -stabilizing elements can effectively increase the ductility of TiAl alloys. Hence, due to the high availability of Ti aluminide alloys these days, the interest in them being fabricated through powder metallurgy techniques (spark plasma sintering) is increasing as these techniques are cheaper than conventional processes [8].

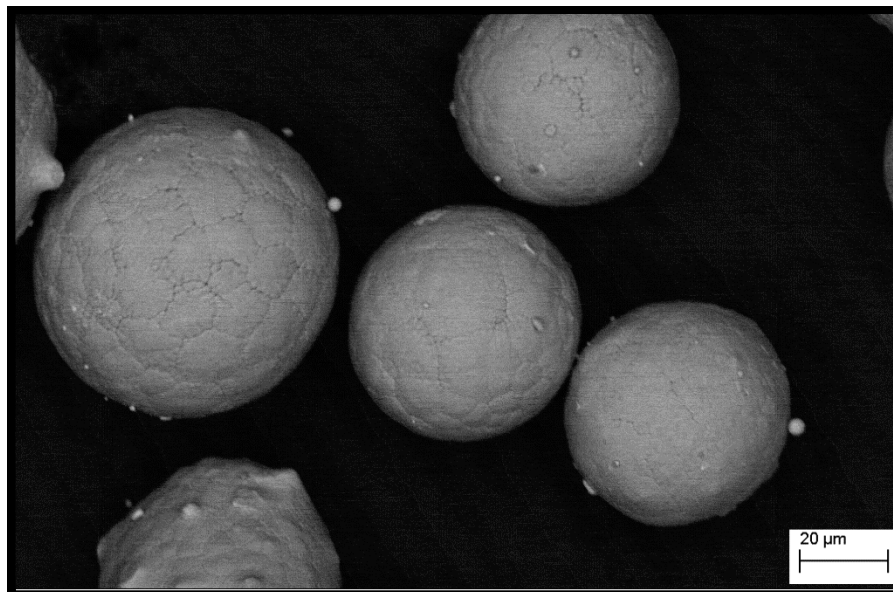
In this research work, an attempt has been made to give an overview of spark plasma sintering of Ti-Al alloys with additions of Mn. A comparative study has been made on the changes in mechanical properties such as density, % of elongation, and hardness with alloying additions. In summary, this study exemplifies the potentials of Ti-48Al-2Cr-2Nb alloy in applications such as aircraft engine components by enhancing its properties.

2. Materials and Methods

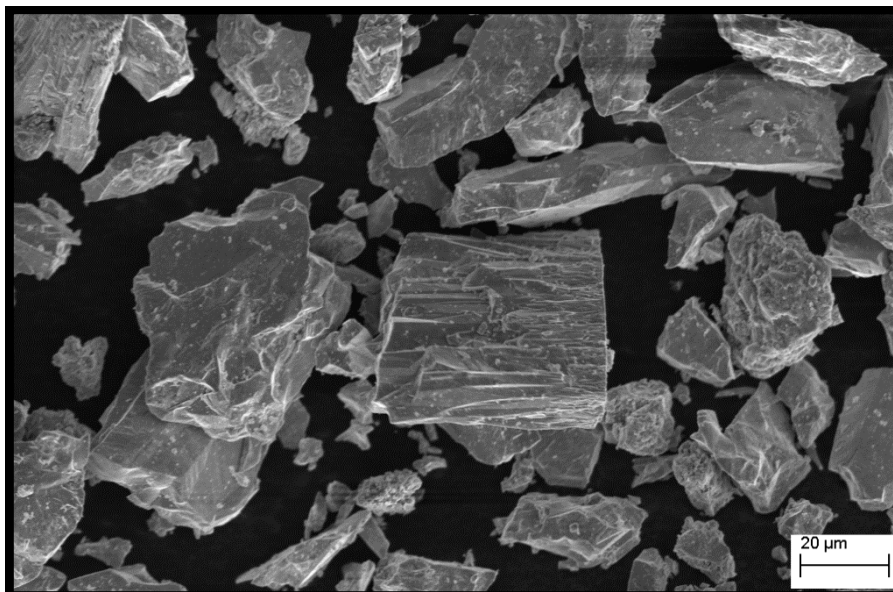
The commercial Ti-48Al-2Cr-2Nb with >99.9% purity powder was purchased from Arcam AB (Sweden) and >99.9% purity manganese (Mn) powder was purchased from Sigma Aldrich India Pvt. Ltd., Bangalore, India. The Ti-48Al-2Cr-2Nb as-received powder morphology is composed of highly uniform spherical $60 \pm 6.1 \mu\text{m}$ -sized particles (as shown in Figure 1a) and Mn particles are irregular in shape with around $30 \pm 5.42 \mu\text{m}$ particle sizes (see Figure 1b). Ti-48Al-2Cr-2Nb alloys with 2.5, 5, and 7.5 wt.% Mn, as well as the alloy without any Mn addition, were blended in the required proportions of elements. The powders were blended for over 25 min using a mortar and pestle for mixing. The characteristics of the powders are presented in Table 1.

Table 1. Characteristics of Ti-48Al-2Cr-2Nb and Mn powders.

Powder	Ti-48Al-2Cr-2Nb	Mn
Particle size (μm)	60 ± 6.1	30 ± 5.42
Purity (%)	~99.9	~99.9
Density (g/cm^3)	3.9	7.3



(a)



(b)

Figure 1. Powder SEM images of (a) Ti-48Al-2Cr-2Nb, (b) Mn.

The samples were sintered by SPS (spark plasma sintering process) (Model: DR. Sinter 21050) at an on/off low voltage (~30 V) and high current (~600 A). The compressing punch is made of graphite. Cylindrical-shaped graphite dies with dimensions of 30 mm inner diameter, outside diameter of 50 mm, and a height of 50 mm were used. A low thickness of the graphite foil (0.15 mm) was used to allow simple expulsion of the sintered sample, embedded between the graphite die's inner surface and the powder. Before sintering, the flushing of argon gas into the spark plasma sintering heater was performed thrice to produce a final vacuum at 2 Pa. Under 50 MPa, uniaxial pressure samples were sintered at 1150 °C with a 100 °C/min heating rate. The holding time at the sintering temperature was 5 min, following which the samples were permitted to furnace cooling. A K-type thermocouple was utilized for estimating the temperature. Graphite felt was utilized to reduce heat loss by radiation. The sintered samples' thickness and diameter were around 4 to 5 mm and 30 mm, respectively.

Theoretical densities and actual densities were calculated using the formulae (Formulas (1) and (2), respectively) mentioned below, as given by the Archimedes method.

Formula (1) (Theoretical Density)

$$\frac{1}{\rho} = \frac{\text{mass fraction of pre-alloyed powder (48Ti48Al2Cr2Nb)}}{\rho \text{ of pre-alloyed powder (48Ti48Al2Cr2Nb)}} + \frac{\text{mass fraction of Mn}}{\rho \text{ of Mn}} \quad (1)$$

Formula (2) (Actual Density)

$$\text{Actual density} = \frac{\text{Actual Mass}}{\text{Actual Volume}} \quad (2)$$

For each alloy, three tensile specimens were prepared from the sintered samples according to the dimensions of the ASTM E-8 standards [9].

To find the tensile strength of the material, a universal tensile testing machine (Instron 8801, Instron; 825 University Ave, Norwood, MA, USA) was used, and experiments were conducted at room temperature. For the microstructural observation, samples were mounted in a hot mounting using bakelite powder. To get the mirror finish of the sample's surface, the grinding was performed on Emery's sheets of increasing grit sizes, viz., 320, 400, 600, 800, 1000, and 1200. Then, cloth polishing using a disc polisher (Make: Bainpol-VT, Chennai Metco Pvt. Ltd. Chennai, India) with both aluminum oxide abrasive suspended in water and plain water was performed. After getting a mirror finish on the sample surface, samples were etched using Kroll's reagent as per ASTM standard E-407 [10]. The micrographs with higher magnification were obtained through a scanning electron microscope (SEM, Zeiss EVO 18, Carl Zeiss, Jena, Germany). The surface morphology of fractured surfaces of tensile samples was observed using the scanning electron microscope (SEM, Zeiss EVO 18, Carl Zeiss, Jena, Germany).

The analysis of phases was conducted using the X-ray diffraction technique with the PAN Analytic X' Pert Pro machine with Cu-K α radiation ($\lambda = 1.54056 \text{ \AA}$). A Bragg's diffraction angle range of 20° to 90° XRD pattern was recorded. The sintered compacts' microhardness was measured using a Vickers' hardness tester (Economet VH-1D, Chennai Metco Pvt. Ltd. Chennai, India) by applying a 0.5 kgf load for 10 s using a standard diamond indenter at an angle of 136°. The indentations did yield results on VH_{0.5} scale. The indentations were made on ten random sample locations. The mean of the observations was taken as the result of each specimen.

3. Results and Discussions

3.1. Densification

For powder metallurgy, the processed product density measurement is important. We aim to achieve the maximum possible density to facilitate effective mechanical properties. Compare the densification responses of Ti-48Al-2Cr-2Nb to the increasing proportions of Mn (2.5%, 5%, and 7.5% by wt.). The alloy does not appear to be modifying the subject. A relative density plot is attained (Figure 2 and Table 2). From Figure 2, it is visible that the relative density increases with an increase in the proportion of Mn in the alloy. The relative sintered density ranges from 87.85% (for pure Ti-48Al-2Cr-2Nb) to 99.99% (for Ti-48Al-2Cr-2Nb with 7.5% by wt. of Mn). A substantial increase (12.86%) in relative density is achieved with just a 2.5% increase in Mn content in the alloy. Moreover, maximum relative density (99.99%) is performed for Ti-48Al-2Cr-2Nb with 7.5% Mn. In pure Ti-48Al-2Cr-2Nb, the relative density of 87.85% is obtained (lowest among the four samples) due to the high amount of porosity resulting from the lack of proper diffusion [11]. Mn, as an activator, can be used to improve the diffusion characteristics of the alloy by lowering its activation energy. The higher the proportion of Mn in the alloy, the lower the energy required for plastic deformation, and the higher the alloy's diffusion coefficient. Mn also acts as a β stabilizer, and the α_2 (Ti₃Al) phase gradually decreases with an increase in Mn content due to the β -stabilizing effect, resulting in smaller grain size

due to the increased proportion of the β phase [12]. These are the reasons for the increased relative density, increasing Mn's proportion in the alloy.

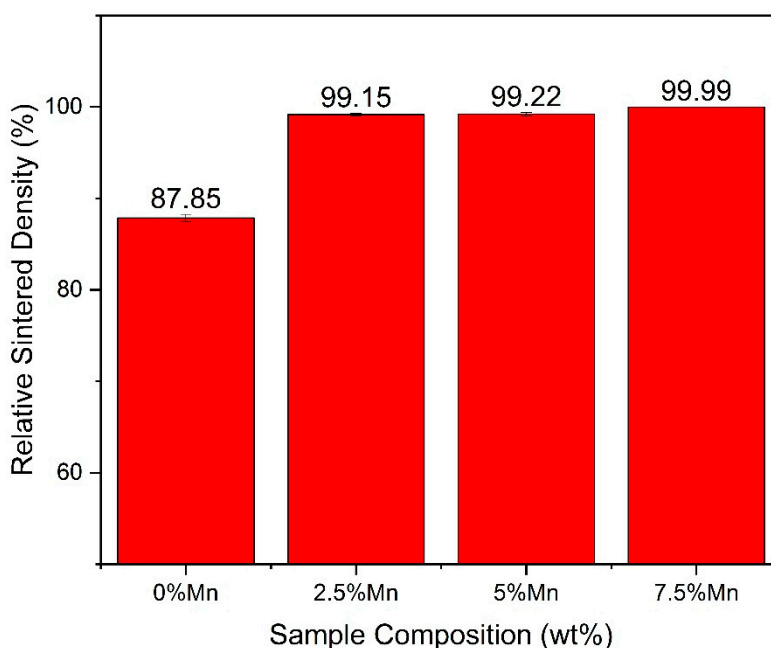


Figure 2. Relative sintered densities of the Ti-48Al-2Cr-2Nb-xMn ($x=0, 2.5, 5, 7.5$ wt.%) alloys.

Table 2. Density of the Ti-48Al-2Cr-2Nb-xMn ($x=0, 2.5, 5, 7.5$ wt.%) alloys.

Composition	Theoretical Density (g/cm ³)	Actual Density (g/cm ³)	Relative Sintered Density (%)
Ti-48Al-2Cr-2Nb	3.9	3.43 ± 0.04	87.86 ± 0.42
Ti-48Al-2Cr-2Nb + 2.5% Mn	3.95	3.91 ± 0.02	99.15 ± 0.15
Ti-48Al-2Cr-2Nb + 5% Mn	3.99	3.96 ± 0.02	99.22 ± 0.18
Ti-48Al-2Cr-2Nb + 7.5% Mn	4.04	4.04 ± 0.01	99.99 ± 0.03

3.2. Phase Analysis

To understand the phase formation in the materials analyzed using XRD, each material's mechanical characteristics depend on the phase present. Figure 3 shows the phases present in the Ti-48Al-2Cr-2Nb + (0, 2.5, 5, 7.5) Mn alloys. Bragg diffraction peaks for γ (TiAl) and α_2 (Ti₃Al) phases were observed in the case of all the samples irrespective of the presence or absence of Mn in the alloys. Nevertheless, no peaks for the Mn-containing phase were observed for any of the samples, suggesting the absence of any Mn intermetallic phase. However, it is observed that the Bragg diffraction peaks shift towards the right with an increase in the proportion of Mn in the alloy. The visible change can be explained by the diffraction relation as stipulated by Bragg and given as $2d \sin \theta = n\lambda$ (here, d = spacing in between planes, θ = angle of diffraction, λ = X-ray's wavelength, and n = number of integers). From the formula as mentioned above, it is obvious that the inter-planar gaps are inversely proportional to the angle of the diffraction peak (θ), i.e., the diffraction peak angle (2θ value) shifts towards the right with the decrease in inter-planar spacing. Gamma (TiAl) and α_2 (Ti₃Al) have a face-centered cubic and hexagonal close-packed crystal structure. Aluminum atoms occupy the upper and bottom layers of a unit cell, and Ti atoms occupy the remaining centers. Manganese atoms dominantly take the place of the aluminum atoms in the lattice [13]. Noticeably, since the atomic radius of the manganese atom (0.127 nm) is less than aluminum's atomic radius (0.143 nm), the occurrence of lattice concentration can happen as aluminum's atomic sites are occupied by those of manganese atoms.

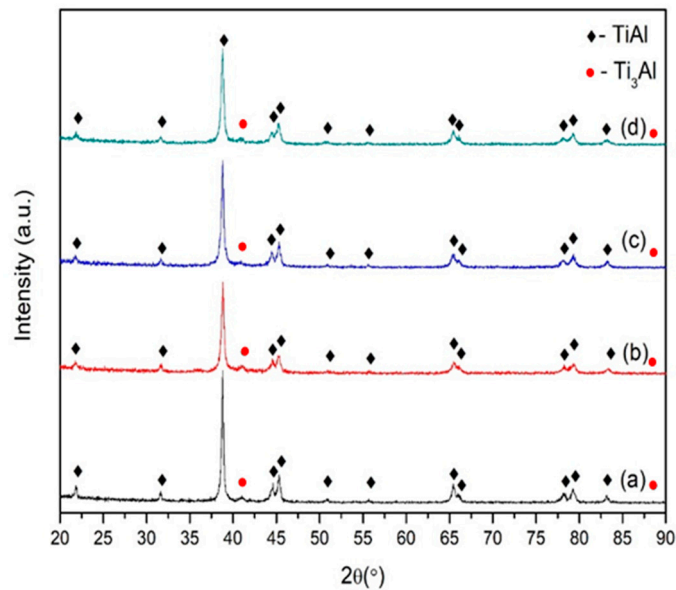


Figure 3. XRD spectra of (a) Ti-48Al-2Cr-2Nb+ 0% Mn, (b) Ti-48Al-2Cr-2Nb + 2.5% Mn, (c) Ti-48Al-2Cr-2Nb + 5% Mn, and (d) Ti-48Al-2Cr-2Nb + 7.5% Mn.

3.3. Microstructure Characterization

Figure 4 shows the scanning electron microscope (backscattered electron mode) images of Ti-48Al-2Cr-2Nb alloy along with the addition of manganese. The samples are observed to have a typical Widmanstatten about-lamellar microstructure, consisting of alternatively arranged lamellae of α_2 and γ phases. The titanium aluminide alloys result in a lamellar structure until the alloy has less than 10% Mn by weight. As the addition of Mn content increases from 0 to 7.5 wt.%, the non-lamellar system becomes evident by the bainite reaction [14]. None of the common variations were found among the four samples analyzed. However, with an increase in Mn's proportion, the β phase became more evident, resulting in a smaller grain size. Its β stabilization effect can explain the jump in the β phase's volume fraction in the alloys with subsequent additions of Mn. Based on previous findings, it is also observed that with the increase in the proportion of Mn, no alteration happened in the lamellar interface features, which stipulates that the separate γ and α_2 morphologies are intact with the addition of Mn [15]. This is also confirmed by the XRD graph shown in Figure 3. Backscattered SEM images showed dark specks of Ti-rich phases, albeit the matrix phase is observed as fairly bright patched areas. A high concentration of each element is seen in the dark regions. As shown in Figure 4c, Ti-laden microstructural proportions comprising small laths are visible. As wt.% of Mn increased in the Ti alloys, Ti-rich areas' sizes were reduced compared to Ti alloy with 5% by wt. of Mn. Observantly, the increase in Mn's content leads to an excellent and uniform distribution of TiAl and Ti₃Al phases.

3.4. Mechanical Properties

The influence of Mn as an additive to the Ti heavy alloy of Ti-48Al-2Cr-2Nb on the microstructure and mechanical properties is analyzed and given in Table 3. From Table 3, it is evident that the % elongation increases with an increase in the quantity of Mn into the sample, thus leading to increased fracture strain as given by Xing et al. (2012) [16], Hwang et al. (1997) [17], and Izumi et al. (1998) [18]. The improvement in the symmetry of the lattice and the increase in the slip systems number can be achieved by adding Mn into the base alloy. It can also be observed from the table that both yield strength and ultimate tensile strength are increased upon Mn's addition. Yield strength increases monotonically with an increase in the proportion of Mn in the alloy. The increase in yield strength due to Mn's expansion can be explained by solid solution strengthening, which is also substitutional. Courtney (2005) [19] found that the addition creates a stress field in the lattice, and the corresponding

solute causes the resistant movement of screw and edge dislocations. So, the yield strength of Mn-added Ti-48Al-2Cr-2Nb is much higher than the base Ti-48Al-2Cr-2Nb.

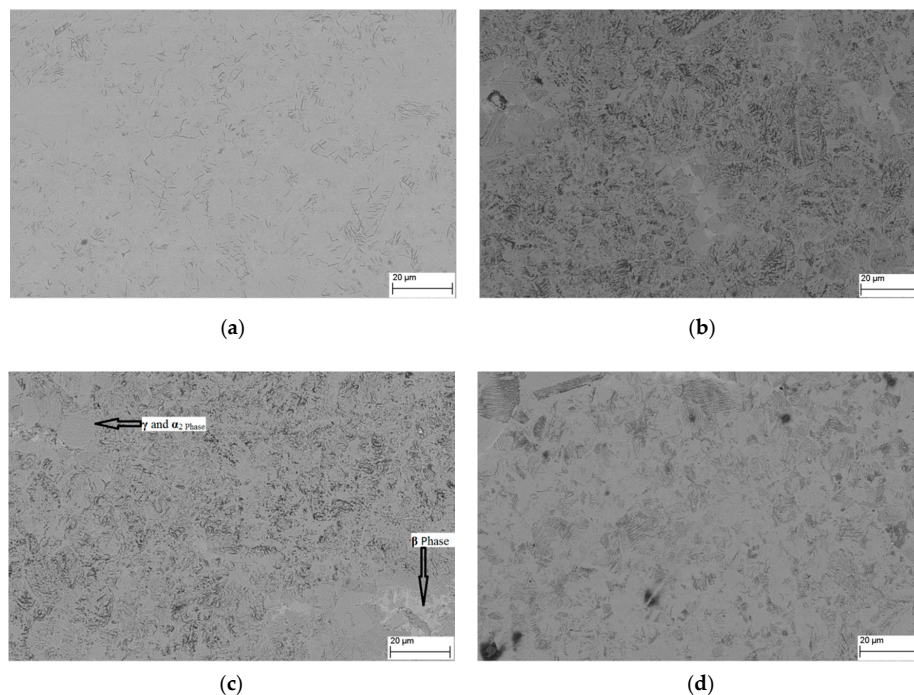


Figure 4. SEM images of (a) Ti-48Al-2Cr-2Nb + 0% Mn, (b) Ti-48Al-2Cr-2Nb + 2.5% Mn, (c) Ti-48Al-2Cr-2Nb + 5% Mn, and (d) Ti-48Al-2Cr-2Nb + 7.5% Mn.

Table 3. Mechanical property analysis of the Ti-48Al-2Cr-2Nb-xMn ($x=0, 2.5, 5, 7.5$ wt%) alloys.

Composition	Yield Strength (MPa)	UTS (MPa)	Elongation (%)	Vickers Hardness (0.5 kgf)
Ti-48Al-2Cr-2Nb	325 ± 6	516 ± 12	1.23 ± 0.2	303.54 ± 14
Ti-48Al-2Cr-2Nb + 2.5% Mn	345 ± 4	819 ± 23	1.7 ± 0.2	353.19 ± 12
Ti-48Al-2Cr-2Nb + 5% Mn	482 ± 9	690 ± 18	1.9 ± 0.1	354.49 ± 08
Ti-48Al-2Cr-2Nb + 7.5% Mn	536 ± 12	570 ± 23	2.1 ± 0.1	368.33 ± 15

The 2.5 wt.% alloy has a higher ultimate tensile strength (UTS) than that of the alloys with 5% and 7.5% Mn. The reduction in UTS with an increase in Mn's proportion is supportively explained by understanding the relative % elongation during the tensile test process. It is known that Mn acts as a β stabilizer, and the volume fraction of the β phase increases with an increase in Mn content. The higher the volume fraction of the β phase, the higher the local stress concentration when propagating a crack in the alloy. This is why the ultimate tensile strength decreases for the increase in Mn's proportion in the alloy. The hardness is found to increase monotonically with an increase in Mn content. The increase in hardness due to Mn's addition can be conferred to the surface at activation and matrix, strengthening Mn's impact on the Ti-48Al-2Cr-2Nb alloy. Due to this reason, the hardness of the samples rises about 20%, with the subsequent increase in the proportion of Mn by 2.5% in the alloy. The incorporation of manganese into the TiAl matrix is the primary responsibility for these alloys' ductility according to the nominal increase in Mn's percentage due to fact that the % elongation could reach the peak at (almost 200% approximately) 7.5 wt.% of Mn. In these cases, the alloy with the highest manganese has higher plastic deformability.

3.5. Fractography

Figure 5 has been used to analyze the reason behind crack initiation, crack propagation, and fracture of the samples in tensile tests. The fracture surface clearly showed a brittle type of fracture. There is no dimple formation in the fracture surface. The fracture surface looks like a transgranular fracture with radial cracks [20]. Inter-lamellar and trans-lamellar facets are formed on the fracture surface based on phase presences [21]. In the trans-lamellar fracture surface, the characteristics show cleavage ridges with a crack propagating direction [22]. In the inter-lamellar fracture, the characteristics show a smooth surface without a crack propagating direction [22]. Figure 5e shows the inter-lamellar surface and trans-lamellar surface inside the blue and red color circles, respectively. It is clear from the figure that the pieces break at the locations where the β phase is present. No observable cracking is formed within the lamella, which confirms that the applied stress is not surpassing the lamellae's loading ability. Crack is initiated due to the presence of the β phase. During tensile testing, the dislocation movements are obstructed by the β phase, resulting in the dislocations' concentration at the interface between the β and lamellar structures, causing increased stress accumulation locally. The local stress allured is much significant and thus higher in value than that of the applied pressure. A micro-crack is visibly formed after the local stress value exceeds a critical and threshold point, amid the β phase. Once a micro-crack is created, its propagation is accelerated by the applied stress. Finally, the sample fractures as soon as the length of the crack reaches a particular threshold value. Thus, highly susceptible to cracking is the sample with the higher β phase proportion. As it is known that with the increase in the proportion of Mn, the volume fraction of the β phase increases as well, the sample with a higher percentage of Mn is more prone to fracture.

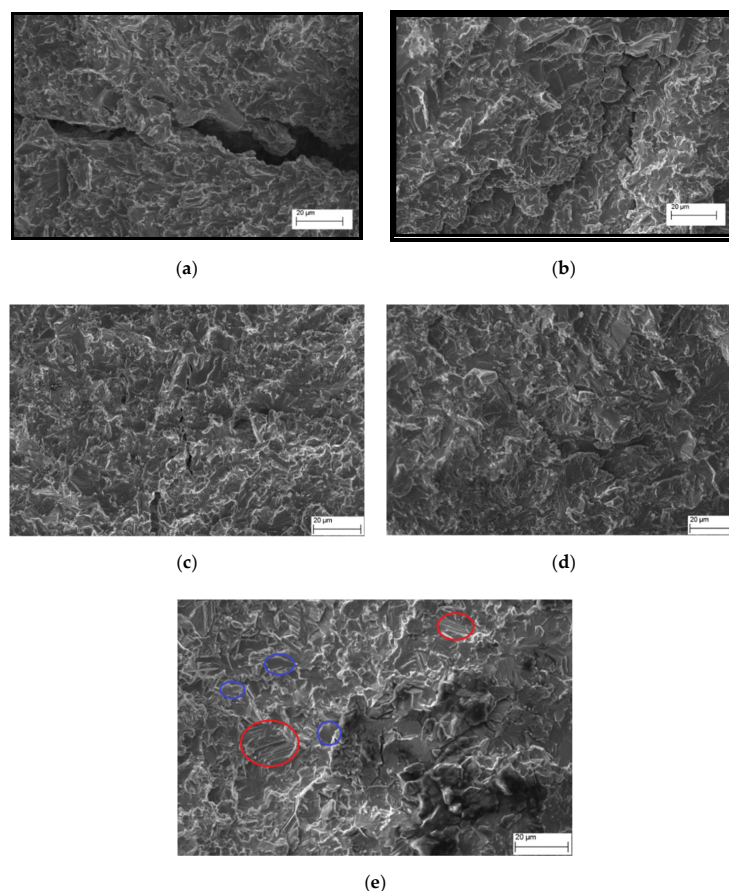


Figure 5. Fractography images of (a) Ti-48Al-2Cr-2Nb + 0% Mn, (b) Ti-48Al-2Cr-2Nb + 2.5% Mn, (c) Ti-48Al-2Cr-2Nb + 5% Mn, (d) Ti-48Al-2Cr-2Nb + 7.5% Mn, and (e) Ti-48Al-2Cr-2Nb + 2.5% Mn. Inter-lamellar surface and trans-lamellar surface inside the blue and red color circles, respectively.

4. Conclusions

In the present work, by varying the Mn content (0 to 7 wt.%) in the pre-alloyed Ti-48Al-2Cr-2Nb powder, four alloys are fabricated using spark plasma sintering at 1150 °C under uniaxial pressure.

It is found that the microstructures and mechanical properties of the Ti-48Al-2Cr-2Nb alloys are significantly affected by the different concentrations of Mn. From the XRD results, except TiAl and Ti₃Al, no other intermetallic phases are not formed with Mn-Ti or Mn-Al in any of the alloys, suggesting that the Mn atoms entirely dissolved in the TiAl alloy. The substitutional solute Mn atoms in the alloy are responsible for the shrinkage lattice parameter of the γ phase.

The yield strength of the alloys is increased monotonically with subsequent additions of Mn separately. It can also be inferred that the trend is caused due to solid solution strengthening of the substitutional solute Mn atoms. High ultimate tensile strength (819 MPa) is observed for the 2.5 wt.% Mn alloy. It is also observed that the alloys' ultimate strengths decreased with an increase in proportions of Mn above 2.5 wt.% in the alloy. Micro-cracks are observed in the fracture surface; the β phase is the preferential site for forming micro-cracks during fracture. Overall, this study throws light on tuning the % of elongation of Ti-48Al-2Cr-2Nb by adding manganese.

Author Contributions: Conceptualization and writing—original draft preparation, A.R.A.; methodology, A.R.A., R.V. and C.-P.J.; data curation, M.S., R.V., M.Y.A. and S.K.P.; investigation, C.-P.J.; writing—review and editing, A.R.A. and C.-P.J. All authors have read and agreed to the published version of the manuscript.

Funding: The authors would like to acknowledge the Ministry of Science and Technology of the Republic of China (Taiwan) under grants MOST 109-2221-E-194-011-MY2 and MOST 107-2221-E-194-024-MY3.

Conflicts of Interest: The authors declare no conflict of interest.

References

- Alman, D.E. Processing and properties of gamma Ti aluminide produced from PREP powders. *Intermetallics* **2005**, *13*, 572–579. [[CrossRef](#)]
- McCullough, C.; Valencia, J.J.; Levi, C.G.; Mehrabian, R. Microstructural analysis of rapidly solidified Ti-Al X powders. *Mater. Sci. Eng. A* **1990**, *124*, 83–101. [[CrossRef](#)]
- Qin, G.W.; Smith, G.D.W.; Inkson, B.J.; Dunin-Borkowski, R. Distribution behavior of alloying elements in α_2 (α)/ γ lamellae of TiAl-based alloy. *Intermetallics* **2000**, *8*, 945–951. [[CrossRef](#)]
- Xia, Y.; Luo, S.D.; Wu, X.; Schaffer, G.B.; Qian, M. The sintering densification, microstructure, and mechanical properties of gamma Ti-48Al-2Cr-2Nb alloy with a small copper addition. *Mater. Sci. Eng. A* **2013**, *559*, 293–300. [[CrossRef](#)]
- Guyon, J.; Hazotte, A.; Bouzy, E. Evolution of metastable α phase during heating of Ti48Al2Cr2Nb intermetallic alloy. *J. Alloys Compd.* **2016**, *656*, 667–675. [[CrossRef](#)]
- Stoloff, N.S.; Sikka, V.K. *Physical Metallurgy and Processing of Intermetallic Compounds*; Springer Science & Business Media: Berlin/Heidelberg, Germany, 2012.
- Gerling, R.; Clemens, H.; Schimansky, F.P. Fundamentals and applications of Ti alloys. *Adv. Eng. Mater.* **2004**, *6*, 23–38. [[CrossRef](#)]
- Kumagai, T.; Nakamura, M. Effects of aluminum content and microstructure on tensile properties of TiAl alloys. *Scr. Mater.* **1996**, *34*, 1147–1154. [[CrossRef](#)]
- Kardak, A.; Bilich, L.; Sinclair, G. Stress Concentration Factors for ASTM E8/E8M-15a Plate-Type Specimens for Tension Testing. *J. Test. Eval.* **2017**, *45*, 2294–2298. [[CrossRef](#)]
- Chemical Composition and Safety Data Sheet, Kroll's Etch/E407/003, Item Numbers: PD1610-105-(250), PD1610-105-(500)*; Waterfall & O'Brien Ltd.: Bristol, UK, 2011.
- Clemens, H.; Lorich, A.; Eberhardt, N.; Glatz, W.; Knabl, W.; Kestler, H. Technology, properties, and applications of intermetallic γ -TiAl based alloys. *Z. Met.* **1999**, *90*, 569–580.
- Kim, J.W.; Hwang, M.J.; Han, M.K.; Kim, Y.G.; Song, H.J.; Park, Y.J. Effect of manganese on the microstructure, mechanical properties, and corrosion behavior of titanium alloys. *Mater. Chem. Phys.* **2016**, *180*, 341–348. [[CrossRef](#)]

13. Wang, Q.; Ding, H.; Zhang, H.; Chen, R.; Guo, J.; Fu, H. Influence of Manganese addition on the microstructure and mechanical properties of a directionally solidified γ Ti-Al alloy. *Mater. Charact.* **2018**, *137*, 133–141. [[CrossRef](#)]
14. Franti, G.W.; Williams, J.C.; Aaronson, H.I. A survey of eutectoid decomposition in ten Ti-X systems. *Metall. Trans. A* **1978**, *9*, 1641–1649. [[CrossRef](#)]
15. Sun, F.S.; Cao, C.X.; Yan, M.G.; Kim, S.E. Alloying mechanism of beta stabilizers in a TiAl alloy. *Metall. Mater. Trans. A* **2001**, *32*, 1573–1589. [[CrossRef](#)]
16. Shu, S.; Qiu, F.; Xing, B.; Jin, S.; Wang, Y.; Jiang, Q. Study of Effect of Mn addition on Ti₂AlC/TiAl composites' mechanical properties through first-principles research and experimental investigation. *Intermetallics* **2012**, *28*, 65–70. [[CrossRef](#)]
17. Lee, T.K.; Mosunov, E.I.; Hwang, S.K. Consolidation of a gamma TiAl–Mn–Mo-alloy by elemental powder metallurgy. *Mater. Sci. Eng. A* **1997**, *239*, 540–545. [[CrossRef](#)]
18. Kawabata, T.; Fukai, H.; Izumi, O. Effect of ternary additions on the mechanical properties of TiAl. *Acta Mater.* **1998**, *46*, 2185–2194. [[CrossRef](#)]
19. Courtney, T.H. *Mechanical Behaviour of Materials*, 1st ed.; Waveland Press: Long Grove, IL, USA, 2005.
20. Lapin, J.; Štamborská, M.; Pelachová, T.; Bajana, O. Fracture behavior of cast-in-situ TiAl matrix composite reinforced with carbide particles. *Mater. Sci. Eng. A* **2018**, *721*, 1–7. [[CrossRef](#)]
21. Wang, J.; Luo, Q.; Wang, H.; Wu, Y.; Cheng, X.; Tang, H. Microstructure characteristics and failure mechanisms of Ti-48Al-2Nb-2Cr titanium aluminide intermetallic alloy fabricated by the directed energy deposition technique. *Addit. Manuf.* **2020**, *32*, 101007. [[CrossRef](#)]
22. Chen, J.H. Brittle Fracture of TiAl Alloy and NiTi Memory Alloy. In *Micro Mechanism of Cleavage Fracture of Metals*; Elsevier: Amsterdam, The Netherlands, 2015; pp. 365–443.

Publisher's Note: MDPI stays neutral with regard to jurisdictional claims in published maps and institutional affiliations.



© 2020 by the authors. Licensee MDPI, Basel, Switzerland. This article is an open access article distributed under the terms and conditions of the Creative Commons Attribution (CC BY) license (<http://creativecommons.org/licenses/by/4.0/>).